Structural and mechanical anisotropy in rheotactically aligned bacterial cellulose

Yvonne Gmach · Daniel Van Opdenbosch

Abstract In this work, we demonstrate the preparation of oriented bacterial cellulose from *Komagataeibacter sucrofermentans* by rheotactic growth in a simple and adaptable setup. The resulting materials were assessed by their yields, geometric densities, and by X-ray diffraction, scanning electron and optical microscopy, and mechanical testing. They exhibited large differences in toughness, resulting from differences in fracture strain or highly anisotropic strengths. Their growth characteristics, structural and mechanical anisotropies and crystalline phase characteristics are discussed and compared to statically grown references and to instances from the literature. Here, we consider the length scales of structural anisotropy in native bacterial cellulose pellicles, and the origin of mechanical anisotropy. Further, we identify a tentative limit on achievable structural alignment in bacterial cellulose, as well as a correlation between crystallinity and disorder in the crystalline phase of bacterial cellulose.

Y. Gmach · D. V. Opdenbosch (✉)
Technical University of Munich, Campus Straubing for Biotechnology and Sustainability,Chair for Biogenic Polymers, Schulgasse 16, 94315 Straubing, Germany
e-mail: daniel.van-opdenbosch@tum.de

Introduction

Bacterial cellulose (BC) is a substance with an immense range of applications, already in use and prospective, as comprehensively reviewed by Ul-Islam et al., Campano et al., Andriani et al. and Pandit et al., amongst others (Ul-Islam et al. 2015; Campano et al. 2016; Andriani et al. 2020; Pandit and Kumar 2021). A snap search using Google Scholar showed 19 reviews concerning BC within the last five years alone. Those older than one year garnered a median of 43 cites per year, illustrating the interest with which this topic is regarded within the materials scientific community.

This is, of course, due to BC's properties. These include a high purity due to its exclusive production from microbial extrusion pores (Ross et al. 1991), good chemical stability, biocompatibility and degradability, and the facility to bind large amounts of water (Campano et al. 2016; Andriani et al. 2020; Pandit and Kumar 2021). In addition, and as outlined in the following, it possesses favourable mechanical properties both in its native wet and dried states. Being originally a hydrogel, they change radically on drying, and in dependence of the manner of drying, providing for a wide range of parameters to investigate. It is therefore all the more surprising that

"somehow no attention had been paid to the physical properties of films until mid-1980s" (Iguchi et al. 2000), when efforts began to rectify this deficiency (Yamanaka et al. 1989).

BC can be produced via cultivation under static or agitated conditions (Ul-Islam et al. 2015; Campano et al. 2016; Andriani et al. 2020; Pandit and Kumar 2021). Static cultures utilize low or no shear power and are the most widely applied method for producing BC pellicles. However, the commercial application of static cultures is limited by their low productivities per volume and time. Agitating a culture aims at overcoming the limiting underlying parameter by supplying oxygen by convection rather than by diffusion through the pellicle itself (Hornung et al. 2006b).

If one wishes to utilize BC as a moldable gel or shapeless suspension, the influence of the cultivation method on the geometry of the originally produced BC is of little concern. This changes, if the aim is to use BC as a monolithic material. Here, agitated culturing methods offer a selection and range of parameters by which one can influence the BC structuring on several length scales. This is enabled by the fact that as-produced BC is characterized by structural hierarchy common to cellulosic materials (Paajanen et al. 2019): On the molecular level, it is semicrystalline (Hermans and Weidinger 1948). On the supramolecular levels, primary aggregates with diameters of 2 nm (Ross et al. 1991; Iguchi et al. 2000) form fibrils with widths of ≈ 100 nm (Franz and Schiebold 1943; Iguchi et al. 2000), which in turn self-assemble into ribbons or bands (Haigler et al. 1982), in a complex multistep process in the extracellular space (Ross et al. 1991).

The lowest hierarchical levels are governed by the manner of production, and typically not influenced by the manner of culturing. However, the formation of either ribbons or bands, also termed 'mats', can already be induced by the composition of the culturing medium (Ohad et al. 1962; Ben-Hayyim and Ohad 1965). On the largest hierarchical levels, the outer shape of the BC monolith typically follows the shape of the culturing vessel (Hornung et al. 2006a). Inbetween, agitated culturing allows to guide the forming BC into a wide variety of arrangements, such as fibrous suspensions or solid balls (Pandit and Kumar 2021).

The archetypal and first described instance (Brown 1886) of monolithic BC is mother of vinegar, a tough and gelatinous membrane growing at the air interface of static vinegar fermentation broth. It solid-phase density in the wet state is typically ≈ 0.01 g $\cdot$ cm^{-3}, and most commonly expressed as its ability to hold about 1 g of water per centigram of cellulose (Pandit and Kumar 2021; Campano et al. 2016). The orientation of cellulose fibrils in a BC pellicle was described by Franz and Schiebold (originally in German) as a "tangled, jumbled network of strands"(Franz and Schiebold 1943). Nevertheless, they observed regions with uniform path differences under crossed Nicols, indicating that locally, fibrils may be aligned parallel.

In wet or dry monolithic BC, the main superstructural features that determine its properties are the solid-phase density and the orientation of cellulose fibrils. 'Properties' are foremost mechanical ones, but may also include optical, absorption, permeation, antimicrobial, etc., as compiled by Campano et al. (2016). Controlling the amount of axial orientation of structural elements in any material affords the possibility to determine the anisotropicity of its properties, in turn allowing to tune them for specific applications. The challenge of producing oriented BC (OBC) was considered by numerous studies. It was achieved

– Chemically by alignment of fibrils in the presence of Na-carboxymethylcellulose (Ben-Hayyim and Ohad 1965), by the addition of a lipid extracted from *Acetobacter xylinum* (Haigh et al. 1973), by prestructuring the growth substrate with oriented polysaccharide chains (Kondo et al. 2002) or, rather remarkably, by static cultivation in an oxygen-permeable silicone tube (Putra et al. 2008)
– Mechanically by direct roll-harvesting from a quasi-static culture (Sakairi et al. 1998), by culturing in a cylindrical fermentor agitated by a rotating vane (Wan et al. 2015) or blade (Luo et al. 2018), or by fixating and drying (Sisson 1935) or wet-drawing statically grown pellicles (Wang et al. 2018)
– Electromagnetically by controlling the movement of *Acetobacter xylinum* (Sano et al. 2010)

Out of these examples, the works of Kondo et al. (2002) and Sano et al. (2010) not only generally guide the cellulose-producing organisms to the locus of BC deposition (e.g. via the availability of oxygen), but directly manipulate the manner in which they move during the material formation. In

general, microorganisms move in specific manners in reaction to a variety of external stimuli, which are then termed chemotaxis, magnetotaxis, phototaxis, etc. Deuerling et al. (2018)

In this work, we consider the phenomenon of rheotaxis, i.e. the movement of microbes in reaction to mechanical forces due to the flow of the surrounding culture medium. Rheotaxis observed in free space, i.e. without solid surfaces, is a combination of mainly microbial morphology, motility, and shear flow (Marcos et al. 2012). In motile flagellated microbes, torque is induced on each cell, directly altering their free-swimming direction, whereas non-motile microbes not in contact with a surface slowly drift (Marcos et al. 2012).

However, when in contact with biofilm under flow, microbes expand along the biofilm, with a preference for regions with high shear (Rusconi et al. 2010; Aufrecht et al. 2019). This directed expansion occurs by a combination of movement and local growth (Aufrecht et al. 2019; Zhang et al. 2010). It is likely aided by a combination of the immediate anchoring of microbes via their cellulose fibrils (Hirai et al. 2002), even during cell division (Yamanaka et al. 1989), and the fibrils and forming pellicles acting as 'fishing' lines or nets, able to capture drifting microbes (Marty et al. 2014). Since the geometry of a viscoelastic biofilm is itself a function of the hydrodynamic conditions (Rusconi et al. 2011) and shear flow-induced torque on rod-like microbial cells leads to their alignment (Luo et al. 2018), we consider microbial expansion along a biofilm under flow a type of rheotaxis.

Wan et al. and Luo et al. already demonstrated the possibility to obtain OBC by flow-shaped growth (Wan et al. 2015; Luo et al. 2018). We hypothesized that it is similarly possible to obtain OBC from a setup that

– Can be constructed from standard laboratory equipment and a small number of components that can be readily manufactured, for example by 3D-printing
– Can be upscaled and parallelized for larger material dimensions and higher total yields
– Produces consistent results regarding the solid-phase density and the orientation of cellulose fibrils

In this article, we demonstrate how these points can be fulfilled. In brief, we adapted the principle of the inclined-plane bioreactor (Doucha and Livansky 1999; Nedbal 2014), by the addition of a controlled-feed nozzle and a series of shear stress- and therefore growth-inducing obstacles. We provide a detailed description of our setup, together with a comprehensive characterization of our materials regarding their anisotropic structural features and mechanical properties, against those of statically grown controls.

Experimental

Sample growth

Microbial strains and chemicals

For all experiments, we utilized the non-motile (Yamada et al. 2012) *Komagataeibacter sucrofermentans* (DSM-15973, German Collection of Microorganisms and Cell Cultures, Braunschweig, Germany). As culturing consumables, we used agar, yeast extract, disodium hydrogen phosphate, citric acid, ethanol absolut (VWR, Darmstadt, Germany), D-(+)-Sucrose, chloramphenicol, peptone from meat (Carl Roth, Karlsruhe, Germany) and sodium hydroxide (Acros Organics, Geel, Belgium).

We used the medium of Schramm and Hestrin (1954), composed of deionized water with 0.5 cg/g peptone, 0.5 cg/g yeast extract, 0.27 cg/g disodium hydrogen phosphate and 0.12 cg/g citric acid, adjusted to an initial of pH 6.5 with 1 M NaOH. 2 cg/g sterile-filtered sucrose was used as the carbon source. The media and all thermally stable components were steam-sterilized for at least 20 minutes at 121 °C. The continuous cultivation of the microorganisms were kept in Petri dishes at 30 °C. For cultivation on agar plates, 1.5 cg/g agar was added to the medium. For the pre-culture, a colony of a 7 days old plate was placed in 200 ml of liquid sucrose medium and incubated statically in a wide-necked flask at room temperature.

Experimental setups

For rheotactic patterning, we constructed inclined-plane bioreactors of our own design as described in the following, together with commercially

available standard components, Fig. 1: peristaltic pump (PLP 380 BT 100-2J, Behr Labortechnik, Düsseldorf, Germany) with hoses (TPP 6.35/9.55 mm & 7.45/11.15 mm, Freudenberg, Weinheim, Germany), 1 l wide-neck bottles with tapped screw cap (GLS 80, Carl Roth), silicone hoses (6.00/2.00 mm & 3.00/1.50 mm, Th. Geyer, Renningen, Germany), sterile filters for air output (ReliaPrep Sterile-EO 0.2 μm, Ahlstrom, Helsinki, Finland) and input (Vent Filter 65 mm PTFE sterile 0.22 μm, GVS Laboratory, Bologna, Italy), flowmeter (generic, 0 to 3 l/min).

Our own components were realized with Solid-Works 2019 and 3D-printed (RepRap X400 Pro V3, Feldkirchen, Germany), or commissioned for 3D-printing (3DBAVARIA, Barbing, Germany) in poly(lactic acid). They consisted of a vegetation area with a partial texture to create shear flow and a nozzle for a spatially and temporally even distribution of the medium from the pulsed jet of the pump over the vegetation area, Figs. 2 and 3. In preliminary tests, we found that a smooth growth plane surface with an initial line of obstacles produced the most homogeneous final material with the most uniform preferred orientation, as determined by optical microscopy.

The bottles were autoclaved in moist heat for at least 20 minutes. The 3D-printed growth areas and nozzles were soaked in ethanol for 3 days before the experiment in order to achieve disinfection. All components were assembled in a sterile bench.

For the production of reference samples via static growth, we used Erlenmeyer flasks closed with cotton-woll stoppers and containing the same culturing medium also used for rheotactic growth. Both the
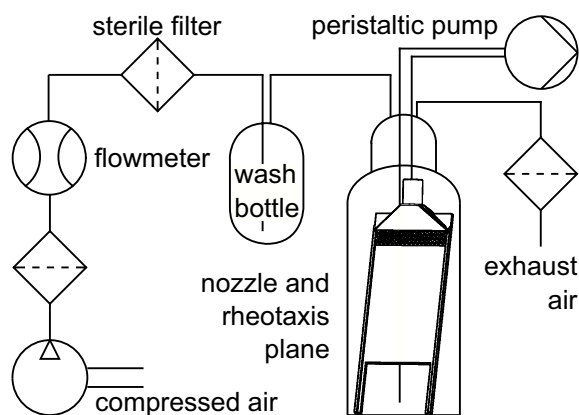

Fig. 2 Left: 3D-printed nozzle clipped onto a growth plane with a width of 6 cm and four lines of obstacles. Right: the same, overgrown with a pellicle of rheotactically oriented BC

static and rheotactic setups are readily scalable by simple size increase, or by parallelization.

Cultivation

Cultivation was carried out at ambient temperature (≈ 22 °C) and relative humidities (39 % < RH < 54 %). To determine the influence of culturing time on the OBC's properties, we performed two types of experiments with total growth periods of 18 days: In type 1, the preculture was 7 days old, and pellicles were grown for 11 days. In type 2, samples were grown for 8 days from a 10 days old preculture. Statically grown reference samples were cultivated according to type 1. To ensure comparability, they
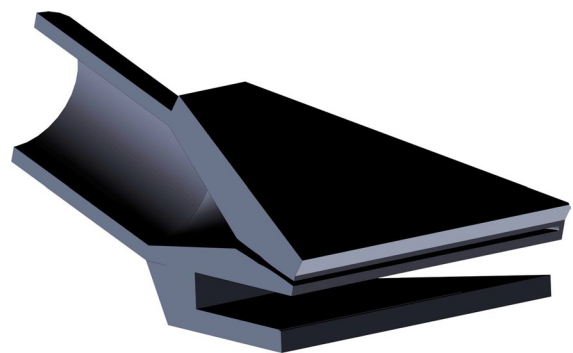

Fig. 1 Flow diagram of the experimental setup.

Fig. 3 Detail drawing of the distribution nozzle

were grown simultaneously from the same culturing batches in medium (1:10).

For rheotactic cultivations, we added antibiotics to counteract potential contaminations from the PLA growth planes. This was achieved by the addition of 1 ml/l of a 34 g/l ethanolic solution of chloramphenicol. The oxygen supply during rheotactic growth was ensured by introducing sterile-filtered compressed air at a flow rate of 1 l/min, humidified by passing through a wash bottle containing desalinated and sterile water, Fig. 1. The exhaust air was also passed through a sterile filter to avoid backflow of aerosols.

Harvesting and characterization

After harvesting, statically and rheotactically grown pellicles were autoclaved in deionized water at 121 °C and 1 bar overpressure for 20 minutes. No further purification, e.g. with NaOH, was carried out and remnants of microbes accepted.

Drying was performed in dependence of the subsequent analyses. Pellicles were kiln-dried at 105 °C for 12 hours to calculate the yielded mass fraction of the carbon source Y. Samples for structural and mechanical analysis were air-dried to a residual moisture of 10 cg/g on acrylic glass.

Thus, we obtained three groups of samples: statically grown BC, and rheotactically grown OBC1 & OBC2 pellicles from the two culturing types 1 and 2.

X-ray diffraction

The data used in this work was obtained from a Bragg-Brentano powder diffractometer (XRD, Miniflex, Rigaku, Tokyo, Japan) with a copper anode, and a silicon strip detector (D/teX Ultra, Rigaku). The setup in detail: goniometer radius 150 mm; both Soller slits 2.5°; divergence slit fixed at 0.625°, but closing variably below 10° 2θ; variable anti-scatter screen; no monochromator; kβ filter 0.06 mm nickel foil; effective receiving slit of the multiline detector 0.1 mm.

The samples were measured in aluminium holders, which were spun during measurements to reduce the effects of preferred in-plane orientation. The data was corrected for incoherent scattering from the holders by subtraction of a blank measurement, scaled by the intensity of the observed Bragg reflexes from aluminium. Residual intensities from these reflexes were

then clipped from the diffractograms. As a measure of quality control of the background correction, we determined that above the angle of discernible Bragg reflexes, the holder-corrected intensities followed the expected progression of the averaged squared atomic scattering factors $\langle f^2 \rangle$ of cellulose, corrected for the Lorentz factor. This angle $\approx 55°$ corresponds to a scattering vector $s = 2\sin\theta/\lambda = 0.6 \text{ Å}^{-1}$, which in polymers is a typical limit for the merging of $\langle f^2 \rangle$ and recorded intensities (Vonk 1973).

The data was evaluated by Rietveld refinement (BGMN, using the Profex interface) (Bergmann et al. 1998; Doebelin and Kleeberg 2015), considering the machine line function, as verified by refining NIST Standards 640e and 660c (silicon and lanthanum hexaboride for peak shapes and positions; machine parameter file and refinement results available from the authors). The scattering angle range $7° < 2\theta < 90°$ was considered, and the sample offset from the goniometer axis refined.

Due to the energy-discriminating detector and the use of an anti-scatter screen and as verified by reference measurements, effectively no inelastic or air scattering was recorded. The holder-corrected diffractograms could therefore be fully deconvolved into coherent and incoherent scattering from the samples. The former were modeled by the crystalline structure as described in the following. The latter were composed of amorphous-phase scattering and crystalline-phase intensities attenuated by thermal or structural disorder. We modeled all incoherent scattering using the sum of a polynomial function and a diffractogram obtained from amorphous cellulose, after confirming its agreement with those reported in the literature (Yao et al. 2020), and using the coefficients and scaling as fitting parameters.

From the spacing between the Bragg-Reflexes at $d_1 \approx 6.1 \text{ Å}$ and $d_2 \approx 5.3 \text{ Å}$, we deduced that the produced cellulose is predominantly of type Iα (Wada et al. 2001). Hence, we used its structure, as determined by Nishiyama et al. (2003) and published by French (2014). Here, the molecular chains run along the unit cell direction $\langle 001 \rangle$.

From preliminary refinements, we determined the simplest physical model leading to consistent results without loss of fitting quality: Only the averaged crystallite sizes $\overline{L}$, the lattice parameters (± 2 %) and a single isotropic thermal diffuse scattering factor were refined.

In X-ray measurements on native cellulosic materials in Bragg-Brentano geometry, the molecular axes are typically aligned within the sample plane (French 2014). Preferred out-of-plane orientation was accounted for by a directional weighting factor W_{hkl}, using spherical harmonics of order $n = 4$ (Ahtee et al. 1989; Bergmann et al. 2001). Exemplary refined patterns are shown as Supporting Information, Fig. S1.

Crystallinities were determined from the measured and Rietveld-refined phase data by the method of Ruland (1961); Vonk (1973). In Vonk's approach, the fractions of the cumulative integrals of the total recorded intensities relative to the cumulative integrals of the intensities of the Bragg reflexes are extrapolated to $2\theta = 0$, thereby accounting for attenuation from the Bragg peaks to the continuous background. Fink et al. first demonstrated its application to ternary systems composed of amorphous cellulose, and cellulose I and II (Fink et al. 1985), emphasizing its theoretical soundness. We applied a lower evaluation limit $s_p = 0.3\ \text{Å}^{-1}$ of the scattering vector s.

The method of Ruland and Vonk also yields values of the sum lattice disorder parameter k (Ruland 1961), which accounts for the combined attenuating effects of thermal vibrational disorder, and lattice disorders of the first and second kinds (Sao et al. 1997). Exemplary patterns evaluated by the method of Ruland and Vonk are shown as Supporting Information, Fig. S2.

Electron microscopy

Samples were sputtered with gold/palladium (SCD050, Bal-tec, Balzers, Lichtenstein) and imaged by scanning electron microscopy (SEM, DSM 940A, Zeiss, Oberkochen, Germany) at an accelerating potential of 15 kV.

Optical microscopy

To quantify preferred orientations within the sample plane, we used an optical microscope (OM, RMA5, Askania Mikroskop Technik, Rathenow, Germany) with a semi-apochromat objective 5x/0.15 (MPlan-FLN, Olympus, Tokio, Japan), a digital camera (EOS 550D, Canon, Tokio, Japan) together providing an observable area of 6.7 mm², and a eucentric rotating stage with azimuth angles of rotation around the sample normal ϕ. Samples were placed fixed between microscopy slides and cover slips and viewed between crossed polarizers without a compensator. Images were recorded in steps of ϕ, at constant white-light illuminance I_0 and shutter times.

For a single birefringent object rotating under crossed polarizers, the expected transmitted intensity is given by Eq. (1). Here, the factor C accounts for the wavelength λ of the setup, and the object's thickness d and birefringence $\Delta n(\lambda)$. Since were interested in the dispersion of molecular orientations only, we used C as an empirical parameter.

$$I(\phi)/I_0 = C\sin^2(2\phi) \tag{1}$$

From each micrograph recorded per step of ϕ, a value of $I(\phi)$ with standard deviation $\sigma(I(\phi))$ was calculated as the arithmetic mean of its brightness values I. The $I(\phi)$ were fitted by Eq. (1) with parameter C as a function of the azimuth angles ϕ in relation to the orientations of the polarizers at which they were recorded. We added a summand D as an empirical parameter to Eq. (1) to account for the offset in $I(\phi)$ caused by the variation $\sigma(I(\phi))$ per micrograph. This allowed us to calculate a measure of orientation O by Eq. (2). A global orientational uniformity parameter $\overline{U}$ was determined as the arithmetic mean of all $U(\phi)$, Eq. (3).

$$O = 2/\pi \arctan(C/D) \tag{2}$$

$$U(\phi) = \sigma(I(\phi))/I(\phi) \tag{3}$$

Mechanical testing

Tensile tests were performed with a universal testing machine (SmartTENS 20, Emmeram Karg Industrietechnik, Krailingen, Germany). They were carried out at an elongation rate of $5.5 \cdot 10^{-3}\ \text{s}^{-1}$. We tested rectangular strips of material with thicknesses $t \approx 50\ \mu\text{m}$ (determined individually using a micrometer screw gauge), widths $w = 1$ cm and lengths $l = 4$ cm, for sample lengths between clamps of $l_0 = 3$ cm. In case of OBC, these strips were cut perpendicular or parallel to the direction of former culturing medium flow. A single grown sample yielded three strips. Twelve strips were measured per type of material and per orientation, in case of OBC.

The resulting curves of force F over displacement Δl were converted to curves of stress $\sigma = F/(t \cdot w)$ over strain $\epsilon = \Delta l/l_0$. They typically showed two

features that complicated their evaluation, namely a gradually decreasing initial upward curvature and a departure from the linear-elastic regime by a gradually increasing downward curvature. After noting that each curve did in fact contain a discernable linear elastic region, these were accounted for by selecting the maximum linear-elastic gradient out of a number of Theil-Sen slopes, which were determined in steps of 100 data points. The intersect of the maximum-gradient Theil-Sen slope with the ordinate was then used to correct the offset of the entire testing curve along the abscissa, thus eliminating any inital 'toes'. The gradient itself was taken as the value of the elastic modulus E.

From the testing curves, we determined the strengths $R = \max \sigma$, the total and plastic deformations at fracture A_t and A, and the total and plastic works of fracture W_t and W, Eqs. (4–6).

$$A = A_t - R/E \tag{4}$$

$$W_t = \int_0^{A_t} \sigma \, d\epsilon \tag{5}$$

$$W = W_t - R^2/(2E) \tag{6}$$

All fitted curves were reviewed graphically to ensure that the determined parameters accurately reflected their progressions, Fig. 4. In no sample did necking occur before fracture. We also performed cyclic tensile tests on each two BC, OBC1 and OBC2 samples. The resulting curves of stress over strain confirmed that recorded departures from the linear-elastic regime constitute permanent plastic deformation, see Supporting Information, Fig. S3.

In order to obtain a measure of mechanical anisotropy, we adapted the theory of Cox for the elasticity of fibrous materials (Cox 1952). Having measured our rheotactically grown materials in two directions perpendicular to one another, we simplified the kernel of the fiber orientational distribution function $\pi f(\theta)$ to include only the first term of the periodic expansion, with coefficient a_1, Eq. 7. Here, θ is the azimuth angle of fiber orientation within the sample plane. A simplified kernel also leads to a simplified form of the Equation for the elastic modulus, Eq. (8) (Cox 1952). In this equation, K is the
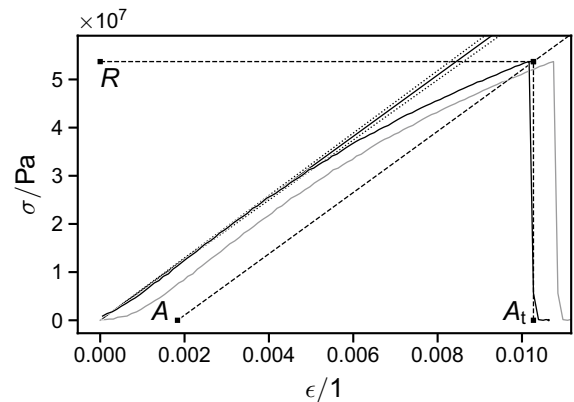

Fig. 4 Typical testing curve showing the original data (gray) and the data corrected by the ordinate intersect of the Theil-Sen slope (also yielding $E = d\sigma/d\epsilon$) to the linear portion of the curve (black). The dotted lines outline the 90 % confidence interval to the Theil-Sen slope

bulk modulus and α is the angle of loading, relative to θ.

$$\pi f(\theta) = 1 + a_1 \cos 2\theta \tag{7}$$

$$E(\alpha) = \frac{2K(2 - a_1^2)}{\left(12 - 2a_1^2 - 8a_1 \cos 2\alpha + 2a_1^2 \cos 4\alpha\right)} \tag{8}$$

We defined the azimuth angle parallel to the growth direction as $\theta = 0$, and all $\alpha := \theta$. Fitting Eq. (8) to sets of two values of E with $\alpha = 90°, 00°$ for testing perpendicular and parallel to the growth directions each, yielded the anisotropy parameters a_1.

Manner of reporting quantities and uncertainties

All experiments and characterizations were performed four times, and their results averaged. While they were performed with great care, we wished to make the reported values robust against unknown sources of error. Hence, we used medians and median absolute deviations to average and provide uncertainties to measurement values or calculation results pertaining to the measurements.

Results

Sample growth

During preliminary experiments, we determined that pellicles were sufficiently stable for harvesting after 5 days. Expectedly, their stability increased with culturing time. Air-dried samples had geometric densities in the range of $0.45 \, \text{g} \cdot \text{cm}^{-3}$ to $0.57 \, \text{g} \cdot \text{cm}^{-3}$, Fig. 5. Considering the strut density of cellulose, this translates to volume fractions of BC between 0.28 and 0.36.

X-ray diffraction

In the Supporting Information, Fig. S2, the accuracy of the background-correction can be discerned by the similar progression of the holder-corrected intensities and the averaged squared atomic scattering factors at high s. In Table 1, we present the materials' XRD-derived crystalline-phase characteristics. Here, the W_{hkl}, whose sum is 1, represent the proportion of the respective lattice plane normals' vectorial components perpendicular to the sample plane.

Electron microscopy

Electron micrographs revealed that all materials are nonwoven fabrics, Fig. 6. They vary in the apparent fiber directionalities, with alignment being discernible in the OBC.

Optical microscopy

Figure 7 shows the orientational parameters obtained from optical microscopy together with those obtained from mechanical testing.

Mechanical testing

For the OBC, mechanical properties are reported perpendicular ⊥ and parallel ‖ to the directions of fiber orientation. Figures 8, 9, 11 and 12 show the determined values of the fundamental mechanical properties tensile strength, elastic modulus, deformations at fracture and works of fracture.

In Figure 10, we plotted the projected progression of $E(\alpha)$ together with the fiber orientational
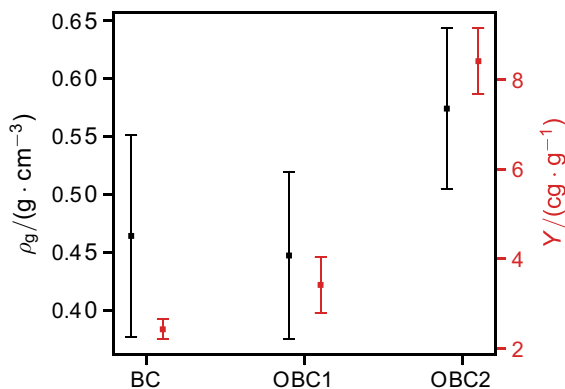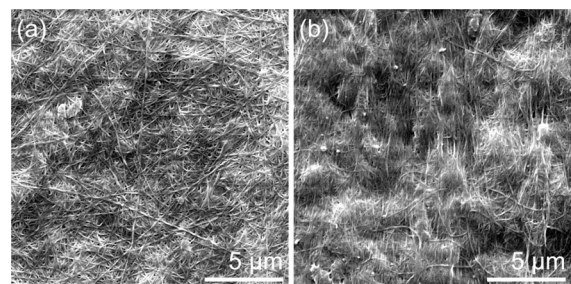

Fig. 5 Averaged geometric densities of the mechanically tested statically and rheotactically grown BC samples, together with the yields of their production methods

Fig. 6 Representative scanning electron micrographs of the internal structures of **a** BC, **b** OBC

Table 1 Structural characteristics of the statically and rheotactically grown BC and OBC: crystallinities x_c, average crystallite sizes $\bar{L}$, sum lattice disorder parameters k, and directional weighting factors W_{hkl}

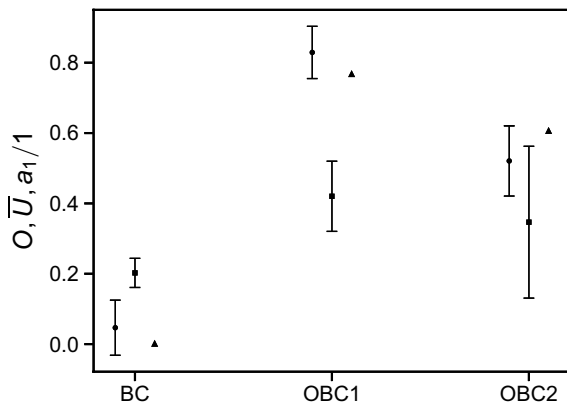| Identifier	$x_c/1$	$\bar{L}/\text{nm}$	$k/\text{Å}^2$	W_{100}	W_{010}	W_{001}
BC	0.83 ± 0.04	8.3 ± 0.5	3.9 ± 2.7	0.78 ± 0.02	0.22 ± 0.01	0.00 ± 0.00
OBC1	0.85 ± 0.02	8.1 ± 0.2	3.6 ± 0.7	0.74 ± 0.01	0.26 ± 0.01	0.00 ± 0.00
OBC2	0.87 ± 0.08	9.0 ± 0.1	5.9 ± 1.8	0.82 ± 0.07	0.18 ± 0.07	0.00 ± 0.00

Fig. 7 Measures of orientational uniformity from optical microscopy O (circles) and $\overline{U}$ (squares), and the anisotropicity parameter a_1 of the elastic moduli (triangles), Eq. (2), (3) & (8)
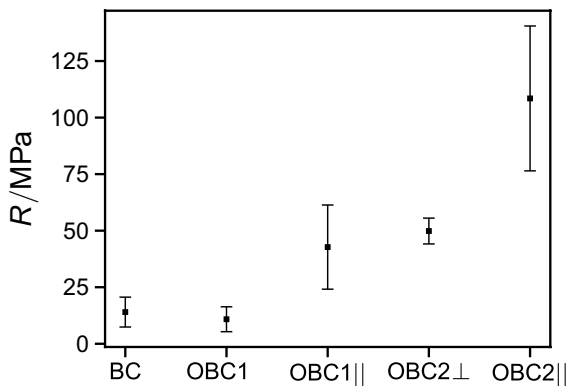
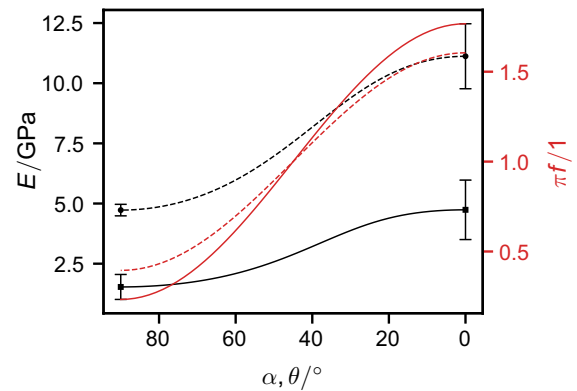

Fig. 10 Elastic moduli of the rheotactically grown BC as functions of loading angle and fitted by Eq. (8), and the fiber orientational distributions as functions of the azimuth angle within the sample plane (red, via Eq. (7)), for OBC1 (squares and full lines) and OBC2 (circles and dashed lines)

Fig. 8 Tensile strengths of the statically and rheotactically grown BC
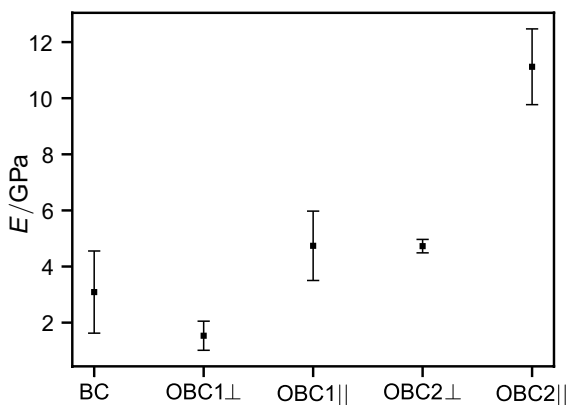
Fig. 9 Elastic moduli of the statically and rheotactically grown BC

distribution function $\pi f(\theta)$. Here, the angles are plotted from 90° to 0° for better visual correlation to Fig. 9.

Discussion

Rheotactic growth characteristics

In preliminary tests, we determined that obstacles on the growth plane are a requirement for the formation of an adherent continuous pellicle. These obstacles create regions of high shear flow, thereby inducing biofilm growth as described in literature (Rusconi et al. 2010; Aufrecht et al. 2019). They also improved the distribution of the liquid over the growth area. We further determined that the homogeneity of the pellicle could be improved by omitting the obstacles downstream of an initial line, as shown in Fig. 2.

In this work, the surface to volume ratios of the growth medium $r_{S/V}$ were 0.35 cm^{-1} for static growth, and 0.79 cm^{-1} for rheotactic growth. We observed that neither the final materials' densities ρ_g nor their yields Y were systematically influenced by the choice of static or rheotactic culturing, Fig. 5. We conclude that the influence of the growth parameter $r_{S/V}$ is overshadowed by other those of other parameters. This is in agreement with literature, where Krystynowicz et al. determined that a $r_{S/V} = 0.71$ cm^{-1} resulted in the highest BC yield, while pointing out that previous

studies hat determined an optimal $r_{S/V} = 2.2$ cm^{-1} (Krystynowicz et al. 2002).

Both ρ_g and Y were, however influenced by the ratio of pre-culturing to growth time, 7 d/11 d for OBC1 and 10 d/8 d for OBC2. The latter led to an increase in ρ_g of ≈ 30 % and Y of ≈ 250 %, illustrating the necessity for multi-parametric optimization of growth systems.

As discussed in the following, the defining feature of the OBC prepared in this work is that their preferred orientations were achieved with little extraneous interaction, i.e. only through gravity-induced flow. Neither detailed pre-structuring of the growth surface (apart from coarse lines of obstacles), nor mechanical intervention by e.g. agitation, roll-harvesting, wet-drawing, nor detailed structural control via chemical or electromagnetic means, as outlined in the introduction, were applied. Instead, directionalities were achieved by the native flow-guided expansion of biofilm starting from and anchored to regions of the substrate exhibiting high shear flow.

Directionalities

During rheotactic cultivation, the acetic acid bacteria are pumped in a circular process, continuously inoculating the growth area and their own biofilm. The bacteria that have settled form a constantly lengthening cellulose pellicle to which they remain connected and that aligns with the direction of flow, leading to the observed structural and mechanical anisotropies.

Early on and based on X-ray diffractograms, Sisson found that cellulose membranes, when pressed into sheets, tend to exhibit selective uniplanar orientations (Sisson 1935). Here, the molecular axes are parallel to, and randomly oriented within the sample plane, with another crystal axis also exhibiting a preferred orientation parallel to the plane. This matches our observed directional weighting factors W_{hkl}, Table 1: The planes {001}, close to normal to the molecular axes, were entirely within the pellicle planes, as generally expected from cellulosic sheets (French 2014). Further, and by contrast to e.g. wood pulp-based papers (French 2014), the planes {010} also showed a preference for in-plane orientation. Our observations are in agreement with those of Sisson, considering that Sisson used a unit cell corresponding to what is now considered cellulose Iβ,

whose direction $\{10\bar{1}\}$ corresponds approximately to {010} in the cellulose Iα used in this work. In Sisson's work, with the beam parallel to the sample plane, this reflex, too, was only faint.

By optical microscopy, Franz and Schiebold determined that small regions of non-stretched cellulose membranes were arranged with preferred orientations, whereas stretched membranes exhibited an overall axiality (Franz and Schiebold 1943). However, neither uniplanar nor uniaxial orientations are typically homogeneously uniform across sample planes. This is illustrated in Fig. 13, where a retardation plate was used to visualize birefringences stemming from local alignments of cellulose: With the former direction of flow during culturing aligned parallel to a polarizer, the interference colors violet/blue and orange/red alternate over patches with diameters in the size range of 10 μm.

To cover a statistically relevant number of heterogeneities, we used OM, providing a larger field of view than SEM-based orientational analyses. In the latter, determining fiber orientations involves analysis and histogramming of angular fiber orientations (Luo et al. 2018), while keeping track of the sample orientation. A typical SEM micrograph will show only $n \cdot 10$ fibers, providing only localized information and necessitating the assessment of a large number of images for a statistic treatment (Luo et al. 2018; Putra et al. 2008).

Orientational analyses using polarized light capture preferred orientations occurring in amorphous and crystalline regions indiscriminately via the total birefringence (Gindl et al. 2006). Considering the standard model of BC production via parallel extrusion out of the cellulose synthase apparatus (van Zyl and Coburn 2019), we assume that both are continuously alternating along-, and therefore aligned to the individual fiber axes.

Putra et al. also applied polarized light microscopy to determine orientations in BC and OBC, with observations matching our own (Putra et al. 2008). They measured the averaged birefringence Δn from different positions on a given sample using a Berek compensator. As demonstrated by Uetani et al., values of Δn can be linearly correlated to measures of structural alignment (Uetani et al. 2019). In our work, the quantity O is a direct measure of the collective orientations of fibers within

the considered micrographs, whereas $\overline{U}$ is a measure of the variation of individual fiber orientations. The quantity a_1, derived from mechanical testing, is a function of the overall orientational distribution function of the fibers. Our expectation that it corresponds to O was confirmed, Fig. 7.

Based on the orientational values O, $\overline{U}$ and a_1, obtained from our setup, we were able to accept our hypothesis: Whereas $\overline{U}$ reflected the expected orientational heterogeneity in all materials, both O and a_1 showed, in agreement with one another, that the rheotactically grown OBC pellicles were indeed oriented. The O and a_1 were rather consistent for all samples per type of material BC, OBC1, OBC2, as expressed by their associated values of uncertainty, Fig. 7.

Bohn et al. used a diffractometer equipped with an Euler cradle to determine degrees of orientation in wet drawn BC pellicles (Bohn et al. 2000). They recorded azimuthal intensities that varied by factors of up to 4. This is remarkably similar to the range of the orientational distribution function πf determined in this work, Fig. 10. They further calculated two measures of orientation normalized to the range [0,1], based on peak half-widths and intensity distributions. The maximum values for either measure were ≈ 0.8, corresponding to the maxima of our O and a_1, Fig. 7. These numbers suggest that there is a limit on achievable cellulose alignment in BC pellicles. From the electron micrographs published by Bohn et al., and shown in Fig. 6, we deduce that this limit stems from intertwining of fibers that cannot be unravelled by drawing or rheotactic growth.

For comparison to orientational histograms, as sometimes given in the literature (Luo et al. 2018), we calculated the proportion of fibers oriented below characteristic angles relative to the direction of flow by cumulative integration and normalization of the distribution functions πf, Fig. 10. For OBC1, proportions of 41 % and 77 % of all fibers were at angles lower than 20° and 45°, respectively. For OBC2 these numbers were 38 % and 72 %.

Directional mechanical properties

More than half of all fibers were oriented within angles of 24° (OBC1) and 28° (OBC2) from the direction of flow in the culturing medium. For comparison, we compiled a selection of reported values of mechanical properties for crystalline and amorphous phases of cellulose, and BC and OBC in Table 2. In the following, we use these values as a basis for discussion.

For BC and OBC each, reported values of R and E differ greatly, as observable even from the selection summarized in Table 2. We traced the Young's modulus of a single BC fiber E_f by two models, one the parallel Voigt, and the other the serial Reuss model (Eichhorn and Young 2001). Both consider their crystallinities x_c, and were expanded to also include -in a simple parametric manner- the preferred orientation of the crystallites' molecular long axes $\langle 001 \rangle$ within the fibers O_c, Eq. (9) and (10). Using the values from Table 2, we found that $E_{f,par} = 80$ GPa for $x_c = 1.02 O_c^2 - 2.29 O_c + 1.79$ and $E_{f,ser} = 80$ GPa for $x_c = 0.08 O_c^2 - 0.17 O_c + 1.06$.

$$E_{f,par} = x_c \big((O_c E_{001} + (1 - O_c) E_{110}) + (1 - x_c) E_{am}$$
(9)

$$E_{f,ser} = \big(x_c / ((O_c E_{001} + (1 - O_c) E_{110}) + (1 - x_c)/E_{am} \big)^{-1}$$
(10)

As pointed out earlier, we assume a near-perfect alignment of cellulose Iα $\langle 001 \rangle$ along each BC fiber axis, $O_c = 1$. Then $x_c = 0.52$ in the Voigt model, and $x_c = 0.97$ in the Reuss model. In this case, we have returned to the equations as applied by Eichhorn and Young, and come to the same conclusion, namely "that the data [of E, in our case the parameter x_c] fall between the two bounds, lying closer to the Reuss lower bound".

Notably, when calculating $E_{f,ser}$ from the values of crystallinity x_c and the overall orientation parameters O determined for the BC and OBC materials in this work, and correcting for the respective material's densities relative to the density of pure cellulose by $E_{f,ser} \cdot \rho_g / \rho_{cell}$, we obtained values of 4.6 GPa, 8.9 GPa and 11.4 GPa for BC, OBC1 and OBC2, respectively. For BC, and the OBC when tested parallel to the growth direction, these correspond only roughly to the values reported in Fig. 9, yet arguably remarkably well, considering the coarseness of our expanded Reuss model.

For BC pellicles, the data from Yamanaka et al. (1989) and Retegi et al. (2010) suggest a positive correlation between R, E and ρ_g. It was also reported that A_t increases with ρ_g (Retegi et al. 2010) and moisture content (Markiewicz et al. 2004). Further, the data compiled in Table 2 indicates that materials with

preferred orientations typically exhibit higher values of A_t.

Hence, R, E and A_t in BC materials can reasonably be expected to depend on fiber density and orientation, which we consider measures of directional fiber connectivity. This notion is supported by Iguchi et al., who –comparing bacterial cellulose to pulp paper– noted that "[i]n the case of bacterial cellulose, the density of inter-fibrillar hydrogen-bonds must be much higher, as the diameter of fibrils is much smaller, and this can be the reason why such a high Young's modulus develops with this material." Iguchi et al. (2000) It as also supported by the current work, where R, E and A_t are positively correlated to the values of ρ_g and O: In both OBC, the directionally averaged R are higher than the isotropic value of BC. Further, both R and E of OBC1 and OBC2 varied by factors of ≈ 2.5 when tested perpendicular or parallel to the predominant fiber orientation. Values of R for broadly comparable non-oriented and oriented cellulosic materials, as collected by Wang et al. (Figure 3e in cited article) (Wang et al. 2018), and for R and E reported by Wan et al. (2015); Luo et al. (2018); Putra et al. (2008) are similarly different in magnitude. While we can not offer an explanation for the lack of increase in A_t from OBC2⊥ to OBC2∥, the differences between BC and the OBC indicate that the fiber connectional density provides BC materials with cohesion over larger lengths of deformation.

The importance of R and the total deformation at fracture A_t lies in their influence on the toughness of materials, of which the total work of fracture W_t is an indicator: In perfectly non-plastic materials $W_t = RA_t/2 = R^2/(2E)$, compare with Eq. (6). If plastic deformation by an amount of A occurs, W_t further increases by its plastic deformation component W. In our own materials, as well as in all reported instances known to us, stress-strain curves of BC materials showed no, or at most minor and debatable, indication of the occurrence of necking (Wang et al. 2018; Sakairi et al. 1998; Cheng et al. 2009; Retegi et al. 2010; Putra et al. 2008; Wan et al. 2015; Luo et al. 2018). Without necking, $W \propto A^x$, where x reflects the steady increase of $\sigma \leq R$ within the plastic deformation regime, observable in the example given in Fig. 4. Examples from literature indicate that the purely elastic deformation regime of BC materials typically ends at $0.5\% \leq \epsilon \leq 1\%$ (Wang et al. 2018; Sakairi et al. 1998; Retegi et al. 2010). This is in agreement with our
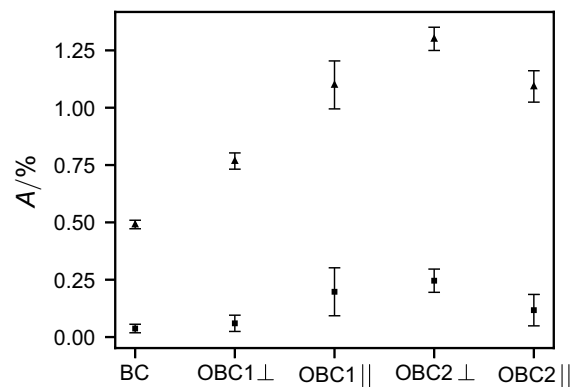

Fig. 11 Plastic A (squares) and total A_t (upward triangles) deformations at fracture of the statically and rheotactically grown BC
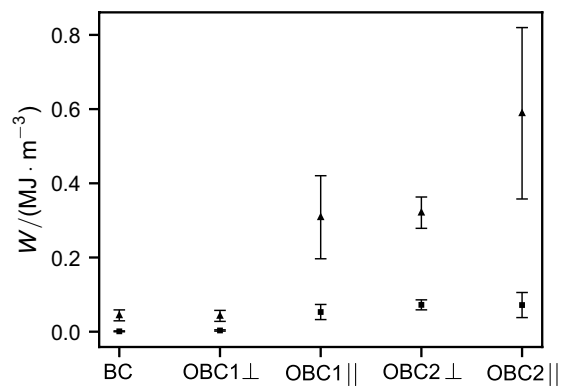

Fig. 12 Plastic W (squares) and total W_t (upward triangles) works of fracture of the statically and rheotactically grown BC

own data, where the amount of elastic deformation at fracture can be traced by the values $A_t - A$ in Fig. 11.

Given this apparent limit for elastic deformation, and the limit on $E \lessapprox 150$ GPa itself (see Table 2), the largest values of W_t are reported for materials that provide for large allowable amounts of plastic deformation, coupled with a large resistance against it Wang et al. (2018). In this study, the three largest values of W_t were achieved in OBC2, and in OBC1∥, i.e. when tested parallel to the fiber orientation. It is notable that OBC2⊥ exhibited similar W_t as OBC1∥. This is most likely due to its larger geometrical density and therefore volume fraction of cellulose, Fig. 5. We assume that it provides a fiber connectional density that exceeds a critical directional threshold for cohesion during plastic deformation.
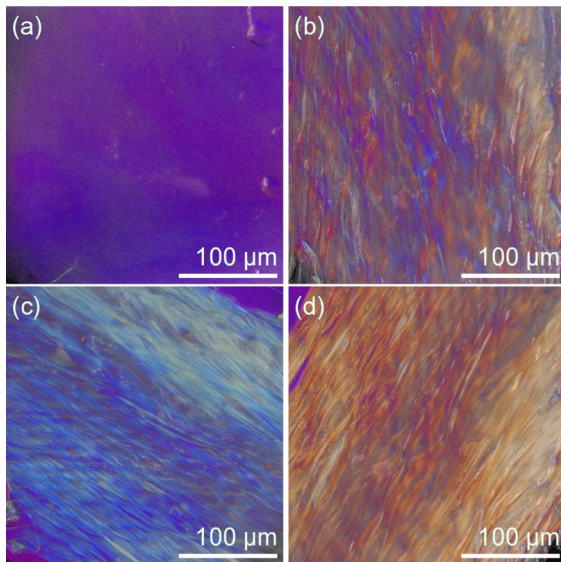
Fig. 13 Polarized light optical micrographs with inserted $\Delta\lambda = 525$ nm retardation plate of (**a**) a statically grown BC pellicle, (**b**) a rheotactically grown OBC pellicle parallel to the polarizers, (**c**) and (**d**) OBC in addition and subtraction orientation to the plate

In case of OBC2‖, W_t are not accompanied by larger A_t, but are due to this material's large directional R, Fig. 8. We expect that further increasing OBC2's ρ_g by altering the cultivation conditions, while outside of the scope of this work, would lead to a further increase of this type of material's toughness.

Crystalline phase characteristics

While less determinant for the properties of BC than its superstructure, the properties of the crystalline phases warrant consideration, since they reveal details about their own production process. Fundamentally, the determined predominant cellulose Iα allomorph meets the expectation from algal-bacterial systems (Wada et al. 2001; Ruan et al. 2016), as do its small crystallite sizes (Imai and Sugiyama 1998; Ross et al. 1991).

Our choice of parameters for Rietveld refinement was based on the requirement that they should not be mutually correlated: The isotropic average crystallite sizes govern reflex broadening, variations in lattice parameters their placement in 2θ, the thermal diffuse scattering factor their attenuation rate with increasing scattering angle, and the directional weighting factors their intensities relative to one another. This choice entails simplifications: For example, in cellulose, both the crystallite sizes and the attenuation rates are certainly anisotropic — but not very. In this example, refining them directionally —or adding further parameters such as structural disorder– would open up a number of possible alternative minima in the optimization process, thereby reducing the robustness of the most important results.

The values of crystallinity x_c reported in this work were similar to BC crystallinity indexes determined by the Segal method (Retegi et al. 2010;

Table 2 Mechanical properties of pure cellulose, and BC and OBC materials. In case of cellulose Iα and OBC, 'Direction' refers to the direction of preferred orientation, adapted to the unit cell orientations published by French (2014)

Type	Direction	R/MPa	E/GPa	A_t/%	References
Iα	$\langle 001 \rangle$		151.7		(Eichhorn and Davies 2006)
	$\langle 110 \rangle$		24.9		
Amorphous	–		6		(Kulasinski et al. 2014)
Single BC fiber	axial		≈ 80		(Guhados et al. 2005; Tanpichai et al. 2012)
Pellicle, wet-drawn & hot-pressed[i]	$\langle 001 \rangle$	1005.3	48.1	4.4	(Wang et al. 2018)
Pellicle, drawn off & air-dried	$\langle 001 \rangle$	311 ± 65	7 ± 2	4.7 ± 1.2	(Sakairi et al. 1998)
Pellicle, freeze-dried & pressed	–	34.1 ± 0.5	2.7 ± 0.1	1.3 ± 0.1	(Cheng et al. 2009)
Sheet Paper[ii]	–	256 85	16.9 4.9	1.7	(Yamanaka et al. 1989)
Films[iii]	–	$(88 \pm 11,$	$(9.8 \pm 0.8,$	$(1.1 \pm 0.1,$	(Retegi et al. 2010)
		$165 \pm 8,$	$10.5 \pm 1.0,$	$2.5 \pm 0.1,$	
		$183 \pm 13)$	$10.6 \pm 0.5)$	$3.8 \pm 0.2)$	

ρ_g : [i] 1.18 g · cm^{-3}, [ii] 0.99 g · cm^{-3}, [iii] $(1.38, 1.44, 1.55)$ g · cm^{-3}

Cheng et al. 2009). However, the results from both methods should be viewed critically. The Segal crystallinity index is a qualitative measure of the proportion of crystalline phase, based on two single values of intensity. While straightforward, its results vary systematically with the crystallite sizes of cellulose, due to the associated reflex broadening (French and Santiago Cintrón 2013). This means that for the purpose of comparison, both quantities should be determined and correlated or discussed, complicating matters.

The method of Ruland and Vonk provides a physically consistent method that considers the entire collected data and accounts for its progression with scattering vector, as well as the attenuation of Bragg peak intensities to diffuse scattering. If a prior Rietveld refinement is used to separate the Bragg intensities from the incoherent and diffuse scattering intensities, structural characteristics such as the crystallite sizes and the rate of attenuation to diffuse scattering are accounted for.

However, both Ruland and Vonk stress that assessing substances with preferred orientations may incur systematic errors (Ruland 1961; Vonk 1973). In our work, we randomized any preferred orientations within the sample plane by spinning. However, this does not account for out-of-plane preferred orientations as exhibited by native cellulosic materials, including the BC studied in this work, Table 1. In our evaluations of cellulose, we observed downward curvatures in plots of the function $R(s_p)$ (Vonk 1973), see Supplementary Figure S2 . We attribute these to the fact that the Bragg intensities from lattice planes $\{hk0\}$ are larger at low s, in proportion to those from $\{00l\}$. This in turn suggests that the values of x_c reported in Table 1 may be systematic over-estimates. We consider any such systematic error to be similar for all our materials, due to their similar amounts of preferred orientation.

Finally, we briefly consider the values of the disorder parameter k. We find that the values of disorder are on average slightly lower than those determined for higher plant fibers (Sao et al. 1997, 1994). Not satisfactorily clear is the correlation between k and x_c in this work, Table 1. In Bohn et al., a slightly positive overall correlation between these two quantities can be discerned (Pearson correlation coefficient of 0.28) (Bohn et al. 2000). Further, their four materials with the largest k were among the six material with the largest x_c, suggesting the presence of a positive general correlation.

Our limited data suggests that increases of k are accompanied by increased average crystallite sizes $\overline{L}$. Cellulose I, when treated with aqueous sodium hydroxide, decreases both in crystallinity and in structural disorder, as determined by Sao et al.: "The disorder parameter (k) initially decreases significantly [...], then increases steadily with the increase in conversion to cellulose II." Sao et al. (1994) Fink and Philipp found the same, and further that the averaged cellulose Iα crystallite sizes increased. They reasoned that "[t]he largest and more perfect cellulose I crystallites are the most resistant ones and even remain in a rather well-ordered state after penetration by alkali"and that "[t]his can be interpreted as an increase in the amount of X-ray amorphous material with increasing degree of lattice transition, while the residual crystalline material simultaneously attains a more perfect order."Fink and Philipp (1985) We speculate that the increase of k with $\overline{L}$ in our materials is due to an inverted mechanism, a type of maturation: Highly ordered initial crystallites may increase in volume only by incorporating additional chain segments from the intercrystalline amorphous phase. Due to restraints on their chain mobility, the added volumes will invariably possess a larger degree of structural disorder.

Outlook

The manner of cultivation assessed in this work combines the relative simplicity of static cultivation with the facility to produce ready-made oriented bacterial cellulose. We consider it a building block, applicable to various approaches for the generation of novel properties in biologically inspired engineering materials. The oriented bacterial cellulose product already contains three key features of load-bearing biological materials, namely multiple levels of hierarchy, a soft-matter phase to facilitate stress dissipation, and structural anisotropy. While this is true for all oriented cellulose materials, we feel that our experimental setup provides a crucial processing advantage: The two main components nozzle and growth plane are 3D printable, and therefore modifiable.

Modifications may be made to include larger levels of hierarchy. By controlling the orientation of

cellulose in relation to larger-scale features, the ability to tune directional mechanical properties can be leveraged (Liu et al. 2020). By analogy to structures found in living nature, microbial biofilms become streamlined when growing rheotactically around obstacles (Rusconi et al. 2010, 2011). Modifications can also be made to allow the introduction of mineralization agents. For example, their sequential introduction may be used to produce nacre-inspired OBC composites, expanding on the example of statically grown nacre-inspired BC composites (Spiesz et al. 2019).

Declarations

References

Ahtee M, Nurmela M, Suortti P, Järvinen M (1989) Correction for preferred orientation in Rietveld refinement. J Appl Crystallogr 22(3):261–268

Andriani D, Apriyana AY, Karina M (2020) The optimization of bacterial cellulose production and its applications: a review. Cellulose 27:6747–6766

Aufrecht JA, Fowlkes JD, Bible AN, Morrell-Falvey J, Doktycz MJ, Retterer ST (2019) Pore-scale hydrodynamics influence the spatial evolution of bacterial biofilms in a microfluidic porous network. PLoS ONE 14(6):e0218316

Ben-Hayyim G, Ohad I (1965) Synthesis of cellulose by acetobacter xylinum: VIII. on the formation and orientation of bacterial cellulose fibrils in the presence of acidic polysaccharides. J Cell Biology 25(2):191–207.

Bergmann J, Friedel P, Kleeberg R (1998) BGMN-a new fundamental parameters based Rietveld program for laboratory X-ray sources, its use in quantitative analysis and structure investigations. Commission of Powder Diffraction. International Union of Crystallography, CPD Newsletter no 20, pp 5–8

Bergmann J, Monecke T, Kleeberg R (2001) Alternative algorithm for the correction of preferred orientation in Rietveld analysis. J Appl Crystallogr 34(1):16–19

Bohn A, Fink HP, Ganster J, Pinnow M (2000) X-ray texture investigations of bacterial cellulose. Macromol Chem Phys 201(15):1913–1921

Brown AJ (1886) On an acetic ferment which forms cellulose. J Chem Soc Trans 49:432–439

Campano C, Balea A, Blanco A, Negro C (2016) Enhancement of the fermentation process and properties of bacterial cellulose: a review. Cellulose 23(1):57–91

Cheng KC, Catchmark JM, Demirci A (2009) Effect of different additives on bacterial cellulose production by acetobacter xylinum and analysis of material property. Cellulose 16(6):1033–1045

Cox H (1952) The elasticity and strength of paper and other fibrous materials. Br J Appl Phys 3(3):72

Deuerling S, Kugler S, Klotz M, Zollfrank C, Van Opdenbosch D (2018) A perspective on bio-mediated material structuring. Adv Mater 30(19):1703656

Doebelin N, Kleeberg R (2015) Profex: a graphical user interface for the Rietveld refinement program bgmn. J Appl Crystallogr 48(5):1573–1580

Doucha J, Livansky K (1999) Process of outdoor thin-layer cultivation of microalgae and blue-green algae and bioreactor for performing the process. Patent US 5(981):271

Eichhorn S, Davies G (2006) Modelling the crystalline deformation of native and regenerated cellulose. Cellulose 13(3):291–307

Eichhorn S, Young R (2001) The Young's modulus of a microcrystalline cellulose. Cellulose 8(3):197–207

Fink HP, Philipp B (1985) Models of cellulose physical structure from the viewpoint of the cellulose I→II transition. J Appl Polym Sci 30(9):3779–3790

Fink HP, Fanter D, Philipp B (1985) Röntgen-Weitwinkeluntersuchungen zur übermolekularen Struktur beim Cellulose-I-II-Phasenübergang. Acta Polym 36(1):1–8

Franz E, Schiebold E (1943) Beiträge zur Struktur der Bakteriencellulose. J Prakt Chem 1(1–6):4–16

French AD (2014) Idealized powder diffraction patterns for cellulose polymorphs. Cellulose 21(2):885–896

French AD, Santiago Cintrón M (2013) Cellulose polymorphy, crystallite size, and the segal crystallinity index. Cellulose 20(1):583–588

Gindl W, Martinschitz KJ, Boesecke P, Keckes J (2006) Changes in the molecular orientation and tensile properties of uniaxially drawn cellulose films. Biomacromol 7(11):3146–3150

Guhados G, Wan W, Hutter JL (2005) Measurement of the elastic modulus of single bacterial cellulose fibers using atomic force microscopy. Langmuir 21(14):6642–6646

Haigh WG, Förster HJ, Biemann K, Tattrie NH, Colvin JR (1973) Induction of orientation of bacterial cellulose microfibrils by a novel terpenoid from acetobacter xylinum. Biochem J 135(1):145–149

Haigler CH, White AR, Brown RM, Cooper KM (1982) Alteration of in vivo cellulose ribbon assembly by carboxymethylcellulose and other cellulose derivatives. J Cell Biol 94(1):64–69

Hermans P, Weidinger A (1948) Quantitative X-ray investigations on the crystallinity of cellulose fibers a background analysis. J Appl Phys 19(5):491–506

Hirai A, Tsuji M, Horii F (2002) Tem study of band-like cellulose assemblies produced by acetobacter xylinum at 4 c. Cellulose 9(2):105–113

Hornung M, Ludwig M, Gerrard AM, Schmauder HP (2006) Optimizing the production of bacterial cellulose in surface culture: evaluation of product movement influences on the bioreaction (part 2). Eng Life Sci 6(6):546–551

Hornung M, Ludwig M, Gerrard AM, Schmauder HP (2006) Optimizing the production of bacterial cellulose in surface culture: evaluation of substrate mass transfer influences on the bioreaction (part 1). Eng Life Sci 6(6):537–545

Iguchi M, Yamanaka S, Budhiono A (2000) Bacterial cellulose-a masterpiece of nature's arts. J Mater Sci 35(2):261–270

Imai T, Sugiyama J (1998) Nanodomains of Iα and Iβ cellulose in algal microfibrils. Macromolecules 31(18):6275–6279

Kondo T, Nojiri M, Hishikawa Y, Togawa E, Romanovicz D, Brown RM (2002) Biodirected epitaxial nanodeposition of polymers on oriented macromolecular templates. Proc Natl Acad Sci 99(22):14008–14013

Krystynowicz A, Czaja W, Wiktorowska-Jezierska A, Gonçalves-Miśkiewicz M, Turkiewicz M, Bielecki S (2002) Factors affecting the yield and properties of bacterial cellulose. J Ind Microbiol Biotechnol 29(4):189–195

Kulasinski K, Keten S, Churakov SV, Derome D, Carmeliet J (2014) A comparative molecular dynamics study of crystalline, paracrystalline and amorphous states of cellulose. Cellulose 21(3):1103–1116

Liu Z, Zhang Z, Ritchie RO (2020) Structural orientation and anisotropy in biological materials: functional designs and mechanics. Adv Func Mater 30(10):1908121

Luo H, Li W, Yang Z, Ao H, Xiong G, Zhu Y, Tu J, Wan Y (2018) Preparation of oriented bacterial cellulose nanofibers by flowing medium-assisted biosynthesis and influence of flowing velocity. J Polym Eng 38(3):299–305

Marcos FuHC, Powers TR, Stocker R (2012) Bacterial rheotaxis. Proc Natl Acad Sci 109(13):4780–4785

Markiewicz E, Hilczer B, Pawlaczyk C (2004) Dielectric and acoustic response of biocellulose. Ferroelectrics 304(1):39–42

Marty A, Causserand C, Roques C, Bacchin P (2014) Impact of tortuous flow on bacteria streamer development in microfluidic system during filtration. Biomicrofluidics 8(1):014105

Nedbal L (2014) Photobioreaktor und Verfahren zur Dünnschichtkultivierung. Patent DE 10 2014 000 691 A1

Nishiyama Y, Sugiyama J, Chanzy H, Langan P (2003) Crystal structure and hydrogen bonding system in cellulose Iα from synchrotron X-ray and neutron fiber diffraction. J Am Chem Soc 125(47):14300–14306

Ohad I, Danon D, Hestrin S (1962) Synthesis of cellulose by acetobacter xylinum: V ultrastructure of polymer. J Cell Biol 12(1):31–46

Paajanen A, Ceccherini S, Maloney T, Ketoja JA (2019) Chirality and bound water in the hierarchical cellulose structure. Cellulose 26(10):5877–5892

Pandit A, Kumar R (2021) A review on production, characterization and application of bacterial cellulose and its biocomposites. J Polym Environ pp 1–18

Putra A, Kakugo A, Furukawa H, Gong JP, Osada Y (2008) Tubular bacterial cellulose gel with oriented fibrils on the curved surface. Polymer 49(7):1885–1891

Retegi A, Gabilondo N, Pena C, Zuluaga R, Castro C, Ganan P, de La Caba K, Mondragon I (2010) Bacterial cellulose films with controlled microstructure-mechanical property relationships. Cellulose 17(3):661–669

Ross P, Mayer R, Benziman M (1991) Cellulose biosynthesis and function in bacteria. Microbiol Rev 55(1):35–58

Ruan C, Zhu Y, Zhou X, Abidi N, Hu Y, Catchmark JM (2016) Effect of cellulose crystallinity on bacterial cellulose assembly. Cellulose 23(6):3417–3427

Ruland W (1961) X-ray determination of crystallinity and diffuse disorder scattering. Acta Crystallogr A 14(11):1180–1185

Rusconi R, Lecuyer S, Guglielmini L, Stone HA (2010) Laminar flow around corners triggers the formation of biofilm streamers. J R Soc Interface 7(50):1293–1299

Rusconi R, Lecuyer S, Autrusson N, Guglielmini L, Stone HA (2011) Secondary flow as a mechanism for the formation of biofilm streamers. Biophys J 100(6):1392–1399

Sakairi N, Asano H, Ogawa M, Nishi N, Tokura S (1998) A method for direct harvest of bacterial cellulose filaments during continuous cultivation of Acetobacter xylinum. Carbohyd Polym 35(3–4):233–237

Sano MB, Rojas AD, Gatenholm P, Davalos RV (2010) Electromagnetically controlled biological assembly of aligned bacterial cellulose nanofibers. Ann Biomed Eng 38(8):2475–2484

Sao K, Samantaray B, Bhattacherjee S (1994) X-ray study of crystallinity and disorder in ramie fiber. J Appl Polym Sci 52(12):1687–1694

Sao K, Samantaray B, Bhattacherjee S (1997) Analysis of lattice distortions in ramie cellulose. J Appl Polym Sci 66(10):2045–2046

Schramm M, Hestrin S (1954) Factors affecting production of cellulose at the air/liquid interface of a culture of acetobacter xylinum. Microbiology 11(1):123–129

Sisson WA (1935) X-ray studies of crystallite orientation in cellulose fibers. II. Synthetic fibers from bacterial cellulose membranes. Division of Cellulose Chemistry, American Chemical Society 89:343–359

Spiesz EM, Schmieden DT, Grande AM, Liang K, Schwiedrzik J, Natalio F, Michler J, Garcia SJ, Aubin-Tam ME, Meyer AS (2019) Bacterially produced, nacre-inspired composite materials. Small 15(22):1805312

Tanpichai S, Quero F, Nogi M, Yano H, Young RJ, Lindström T, Sampson WW, Eichhorn SJ (2012) Effective Young's modulus of bacterial and microfibrillated cellulose fibrils in fibrous networks. Biomacromol 13(5):1340–1349

Uetani K, Koga H, Nogi M (2019) Estimation of the intrinsic birefringence of cellulose using bacterial cellulose nanofiber films. ACS Macro Lett 8(3):250–254

Ul-Islam M, Khan S, Ullah MW, Park JK (2015) Bacterial cellulose composites: synthetic strategies and multiple applications in bio-medical and electro-conductive fields. Biotechnol J 10(12):1847–1861

Vonk CG (1973) Computerization of Ruland's X-ray method for determination of the crystallinity in polymers. J Appl Crystallogr 6(2):148–152

Wada M, Okano T, Sugiyama J (2001) Allomorphs of native crystalline cellulose i evaluated by two equatorial d-spacings. J Wood Sci 47(2):124–128

Wan Y, Hu D, Xiong G, Li D, Guo R, Luo H (2015) Directional fluid induced self-assembly of oriented bacterial cellulose nanofibers for potential biomimetic tissue engineering scaffolds. Mater Chem Phys 149:7–11

Wang S, Chen C, Kong W, Zhu S, Dai J, Diaz AJ, Hitz E, Solares SD, Li T, Li T et al (2018) Transparent, anisotropic biofilm with aligned bacterial cellulose nanofibers. Adv Func Mater 28(24):1707491

Yamada Y, Yukphan P, Vu HTL, Muramatsu Y, Ochaikul D, Tanasupawat S, Nakagawa Y (2012) Description of komagataeibacter gen nov with proposals of new combinations (acetobacteraceae). J General Appl Microbio 58(5):397–404

Yamanaka S, Watanabe K, Kitamura N, Iguchi M, Mitsuhashi S, Nishi Y, Uryu M (1989) The structure and mechanical properties of sheets prepared from bacterial cellulose. J Mater Sci 24(9):3141–3145

Yao W, Weng Y, Catchmark JM (2020) Improved cellulose X-ray diffraction analysis using fourier series modeling. Cellulose 27:5563–5579

Zhang C, Kang Q, Wang X, Zilles JL, Müller RH, Werth CJ (2010) Effects of pore-scale heterogeneity and transverse mixing on bacterial growth in porous media. Environ Sci Technol 44(8):3085–3092

van Zyl EM, Coburn JM (2019) Hierarchical structure of bacterial-derived cellulose and its impact on biomedical applications. Curr Opin Chem Eng 24:122–130